Hyperspectral Imagery Throughput and Fusion Evaluation over Compression and Interpolation

James Patrick
Air Force Research Lab &
Wright State University
WPAFB, OH 45433
james.partick@wpafb.af.mil

Ryan Brant
Wright State University
Dayton, OH
brant.5@wright.edu

Erik Blasch
Air Force Research Lab &
Wright State University
WPAFB, OH 45433
erik.blasch@wpafb.af.mil

Abstract – *Hyperspectral Imagery (HSI) is an emerging capability that extends the analysis of multi-spectral imagery (MSI) through additional bands, variable frequency band distributions, enhanced collections, and improved resolution. These developments have also led to increasing large data files that require intelligent strategies to perform throughput data reduction without degrading exploitation performance. In this paper, we explore the (1) common compression techniques with a novel method that improves the baseline, (2) exploitation targeting with frequency fusion of results over bands to maintain detection, and (3) demonstrate an information fusion performance model strategy for dynamic sensor management of HSI exploitation. The paper describes a method for robust HSI performance evaluation to truncate disturbances, interpolate data across these locations, compress and reconstruct the signal, perform decision-fusion detection, and check the error associated with these operations – all supporting techniques to enable realizable HSI tracking and identification solutions.*

Keywords: HSI, Compression, Detection, Fusion, Robustness, Performance Models, Fusion Evaluation
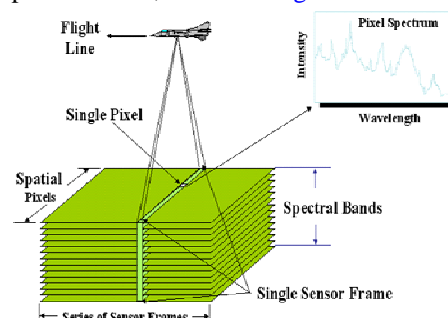
1   Introduction

Hyperspectral Imaging (HSI) has grown as a popular sensor for resource management, agriculture and mineral exploration, environmental monitoring and target identification (ID). The spectral detail provided by HSI provides the ability to distinguish virtually all materials by comparing the waveforms of the image spectrum to those of known substance spectra.

HSI detection analysis has progressed over many years from the geoscience community [1] for agricultural analysis (e.g. see lifetime of work from Landgrebe [2, 3, 4]). Remote sensing applications typically have a large ground sampling distance (GSD), however current developments are decreasing the GSD through higher-resolution systems or varying altitude platforms.

In recent years, there has been substantial interest in HSI target detection [5] with methods such as Support-Vector Machines (SVM) [5], stochastic mixture modeling [6], expectation-maximization [7], and fuzzy-logic fusion [8]. While there is increasing interest in applications such as detection, HSI utilization requires methods to *compress*

the 3D data [9-13], selective frequency fusion for object ID, fast registration for object tracking, and the ability to process frequency bands that are corrupt. This paper documents ongoing compression performance efforts to utilize HSI for object tracking and ID.

Hyperspectral images are produced by instruments called imaging spectrometers. These sensors are typically mounted to high altitude survey vehicles and collect image data simultaneously in dozens or hundreds of narrow adjacent spectral bands, shown in Figure 1.

Figure 1. HSI Collection

Evaluation of HSI fusion systems includes (1) metrics, (2) processing and database constraints, and (3) robustness to operational conditions. The five basic fusion system metrics include throughput, timeliness, accuracy, cost, and confidence. Timeliness and throughput are related to the large HSI file sizes requiring intelligent compression techniques. Accuracy and confidence relate to target detection/ID.[14] Important to *frequency-band fusion* is the quality and size of the data. Throughput and cost (i.e., sensor coverage) are system constraints. A measure of operational *robustness* can be assessed as a system sensitivity to varying operational conditions (i.e. sensor, target, and environment). While many HSI algorithms have been proposed, (e.g. joint compression and classification for stationary target analysis [15]), the goal is to simultaneously determine tradeoffs.

This paper proposes a methodology for joint HSI compression, frequency-interpolation, and exploitation for sensor management. Section 2 overviews HSI processing. Section 3 describes the interpolation across band distortions and Section 4 describes compression techniques. Section 5 presents results and Section 6 lists the discussion and conclusions.

1. REPORT DATE **JUL 2008**	2. REPORT TYPE	3. DATES COVERED **00-00-2008 to 00-00-2008**
4. TITLE AND SUBTITLE **Hyperspectral Imagery Throughput and Fusion Evaluation over Compression and Interpolation**		5a. CONTRACT NUMBER
		5b. GRANT NUMBER
		5c. PROGRAM ELEMENT NUMBER
6. AUTHOR(S)		5d. PROJECT NUMBER
		5e. TASK NUMBER
		5f. WORK UNIT NUMBER
7. PERFORMING ORGANIZATION NAME(S) AND ADDRESS(ES) **Air Force Research Lab &,Wright State University,Wright Patterson AFB,OH,45433**		8. PERFORMING ORGANIZATION REPORT NUMBER
9. SPONSORING/MONITORING AGENCY NAME(S) AND ADDRESS(ES)		10. SPONSOR/MONITOR'S ACRONYM(S)
		11. SPONSOR/MONITOR'S REPORT NUMBER(S)
12. DISTRIBUTION/AVAILABILITY STATEMENT **Approved for public release; distribution unlimited**		
13. SUPPLEMENTARY NOTES **11th International Conference on Information Fusion, June 30 ? July 3, 2008, Cologne, Germany.**		
14. ABSTRACT **see report**		
15. SUBJECT TERMS		

16. SECURITY CLASSIFICATION OF:			17. LIMITATION OF ABSTRACT	18. NUMBER OF PAGES	19a. NAME OF RESPONSIBLE PERSON
a. REPORT **unclassified**	b. ABSTRACT **unclassified**	c. THIS PAGE **unclassified**	**Same as Report (SAR)**	**8**	

2   HSI Processing

The quantity of data associated with a HSI of a given area is very large. Thus to transmit this data back to ground locations for data processing requires large bandwidth or time. Hyperspectral images are amalgamations of images of the same object or area from multiple sensors (spectrometers) simultaneously in dozens or hundreds of narrow adjacent spectral bands. An analogous description would be to visualize a stack of photos of the same object, each only taken at a specific radiance frequency or wavelength (spectrum). Each image is the radiance response of the data (Figure 1).

There are several factors which affect the quality of the signal such as illumination, topography, spectra mixing, resolution and sensor effects. [2] Algorithms exist to address these factors when identifying constituent materials but are typically addressed on a case-by-case basis. [5] One factor existent in nearly all cases and typically uniform is *atmospheric effects*, even for a relatively clear atmosphere. For certain wavelengths these interactions attenuate the amount of incoming energy reflected by the ground to an airborne or satellite sensor. The atmospheric disturbances add variable distortions to the images at particular wavelengths that effect classification.

Water is a major constituent in the atmosphere that absorbs light. The degree to which this occurs depends on the water abundance and the particular wavelength, shown in Figure 2 as various reflectance reductions over different environmental (i.e. background) objects.
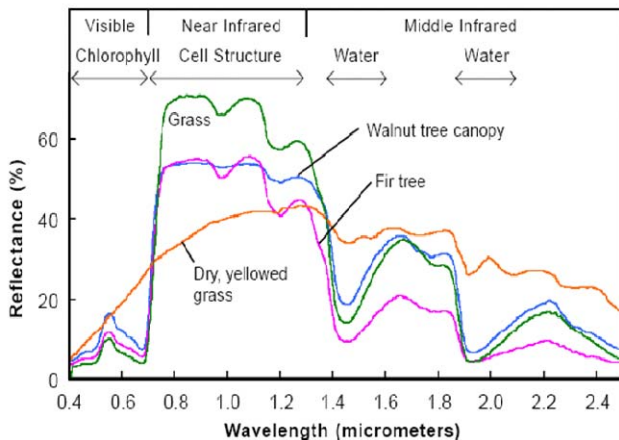

Figure 2. HSI Spectrum (water absorption).

Received signals at certain wavelengths contain such a low signal to noise (SNR) ratio due to this absorption that information is lost. Typically, these wavelengths are cut out before further processing. Truncation of this data leaves a gap in the information that will result in the introduction of high frequency noise when the signal is compressed. This can be avoided by filling this gap with interpolated data. Two well known interpolating polynomials that are used to interpolate the cuts are a cubic spline and a piecewise cubic Hermite polynomial discussed in Section 3.

There is debate on which compression algorithms should be used for accurate HSI exploitation. [10] A standard example is the Discrete Cosine Transform (DCT) which reduces the amount data (an equivalent goal of information fusion). This transform coding relies on the idea that image pixels have a level of *correlation* with neighboring pixels. This correlation can be used to predict values of neighboring pixels, i.e. redundancies in the data will allow image data compression. The DCT attempts to decorrelate the image data and describe the data through a series of transform coefficients.[16, 17] These coefficients are transmitted and the image is reconstructed from these coefficients. Error can be assessed if the full original signal is available, which is explained in Section 4.

After adjustments for sensor, atmospheric, and terrain effects are applied, these image spectra can be compared with field or laboratory reflectance spectra in order to recognize and map surface materials such as particular types of vegetation or diagnostic minerals and identify targets of interest.

2.1 Hyperspectral Data

Remote sensing applications have utilized both multi-spectral imaging (MSI) and hyperspectral imaging (HSI) to accomplish individual application requirements. The characteristic differences between MSI and HSI systems are very important for selection criteria for applications. Typically MSI systems have a smaller range of spectral bands (3-10 spectral bands) than HSI, which can have over 100. Also, MSI systems have wide and irregular spaced spectral bands while HSI systems have their spectral bands wide and regular spaced. Due to the wide spectral band, the amount of information that results in data collection can increase quite dramatically depending on the scene size.

Two examples of HSI imaging systems are Airborne Visible/Infrared Imaging Spectrometer (AVIRIS) and HYperspectral Digital Imagery Collection Experiment (HYDICE). AVIRIS was designed and constructed by NASA's Jet Propulsion Laboratory in 1987 and is associated earth science community for geology, land cover, and natural resource applications. [18] AVIRIS is regarded as having the highest SNR ratio systems around AVIRIS has a 200-mm diameter aperture with a 0.6 rad field of view and 224 spectral channels between the wavelengths of 360nm to 2510nm. The system has high-altitude applications (about 20 km above the ground) with 20m ground resolution. [18].

The NASA AVIRIS data set of Moffet Field (available at http://aviris.jpl.nasa.gov/html/aviris.freedata.html) [19]. The data includes urban information such as buildings, runways, and vehicles collected over a variety of bands. Additional environmental ancillary *environmental models* include: vegetation and water absorption. Figure 3 shows the image cube available for the AVIRIS data (flown at 20K meters over Moffett Filed, CA, USA).
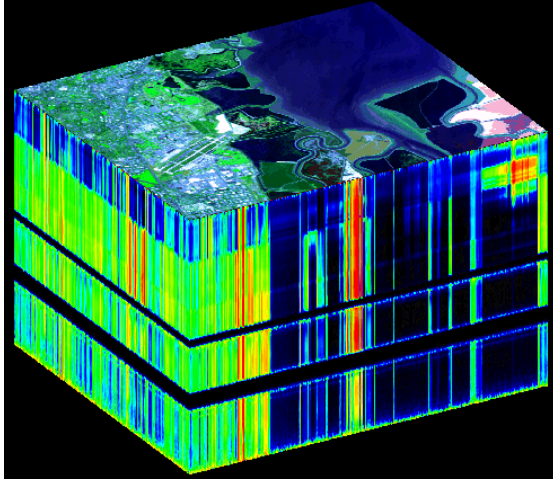
Figure 3. HSI Cube [19].

From the *AVIRIS website*: [19], the top of the cube is a false-color image made to accentuate the structure in the water and evaporation ponds on the right. The sides of the cube are slices showing the edges of the top in all 224 of the AVIRIS spectral channels. The tops of the sides are in the visible part of the spectrum (wavelength of 400 nms), and the bottoms are in the infrared (2,500 nms). The sides are pseudo-color, ranging from black and blue (low response) to red (high response). While the urban and water areas of separable, note the red (700 nm) in the lower right, which is indicative of red brine shrimp targets in the evaporation pond. [18]

HYDICE was built under contract for the Naval Research Laboratory in 1994 and was made available for civilian R&D communities. This system was one of the first low altitude systems which made high spatial resolution possible (around 1m resolution at a 2-km altitude). The aperture size is 2.54cm with a 0.15 rad field of view. There are 210 spectral channels covering the wavelengths between 400nm to 2500nm.

For an airborne platform flying above the Earth's surface there are several items that can cause problematic distortion in certain bands. The most prevalent is the atmosphere. Due to the rotation and vibration of atmospheric molecules in response to certain wavelengths of light, the information obtained in certain bands can become useless due to disruptive interference. These distorted bands are deleted, since they offer no reliable information. There were four regions in the AVIRIS data that were removed due to atmospheric distortion {1:3 μm, 107:114 μm, 153:168 μm, 222:224 μm}. The HYDICE dataset took a different approach by interpolating across the noisy and junk bands.

To utilize these data sets for information fusion throughput and classification performance analysis, a way to deal with the deleted spectral bands that affect performance accuracy requires an interpolation method.

3 HSI Preprocessing (Interpolation)

Atmospheric interference from gas and water result in low SNR ratio in the reflectance signal. This results in large dips in the data. These dips are truncated, performed at specific known frequencies, from the data since they contain little useful information and contribute high frequency noise during the compression process. The gaps left by this truncation are then filled using interpolation [20].

Two well known piecewise cubic interpolating polynomials *cubic-spline* and *Piecewise Cubic Hermite Interpolation* (PCHIP) are used to interpolate across the gap left by data truncation. These numerical algorithms fit data by defining the slope at the local area of interest via piece wise cubic interpolation. Spline requires that the data have a continuous second derivative. PCHIP only requires the first derivative to be continuous. Thus, absence of the second derivative may imply the curvature is discontinuous. PCHIP guarantees the preservation of the shape, as shown below.

The *cubic-spline* (CS) interpolates the data by fitting a third degree polynomial across each interval extending between two consecutive data points, and matches the first and second derivatives of adjacent polynomials at the seams. Thus, the CS provides a continuous function with first and second derivatives [21]. The ith is expressed in the following form

$$P_i^3(x) = [(a_i\,(x-x_i) + b_i)\,(x-x_i) + c_i]\,(x-x_i) + f(x_i) \quad (1)$$

where x represents points where data is taken with $i = 1,\dots, N$. The coefficients of the slopes a, c are given by are given by Eq's.(2) and (3)

$$a_i = \frac{b_{i+1} - b_i}{3\,h_i} \quad (2)$$

$$c_i = \frac{f(h_{i+1}) - f(x_i)}{h_i} - \frac{h_i\,(b_{i+1} + 2\,b_i)}{3} \quad (3)$$

where $h_i = x_{i+1} - x_i$. Substituting Eq's. (2) and (3) into the cubic polynomial, Eq. (1) renders

$$\frac{h_i b_i}{3} + \frac{2(h_{i+1} + h_i)\,b_{i+1}}{3} + \frac{h_{i+1}\,b_{i+2}}{3}$$
$$= \frac{f(x_{i+2}) - f(x_{i+1})}{h_{i+1}} - \frac{f(x_{i+1}) - 2\,f(x_i)}{h_i} \quad (4)$$

Eq. (4) results in a set of equations that form a tridiagonal matrix that can then be solved for the coefficients b_i. Closure conditions are necessary as this system is over-specified, i.e. system is singular without them.

The PCHIP interpolation function in Eq.(5) is found by finding the coefficients given by Eq's.(6,7)

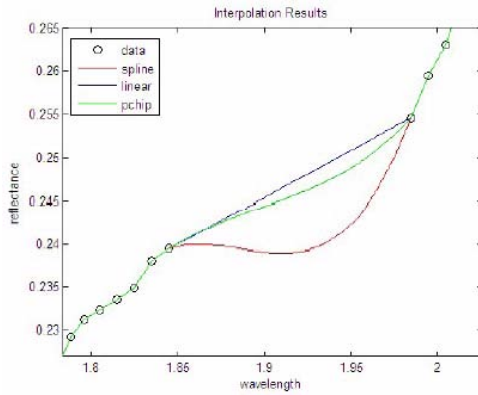$$P_3(x) = f(x_i)\,h_{i;0}(x) + f(x_{i+1})h_{i+1;0}(x)$$

$$+ \, m(x_i) \, h_{i;1}(x) + m(x_{i+1})h_{i+1;1}(x) \qquad (5)$$

$$
\begin{aligned}
h_{i;0}(x) &= H_{i;0}(\xi) \\
h_{i;1}(x) &= (x_{i+1} - x_i) \, H_{i;1}(\xi)
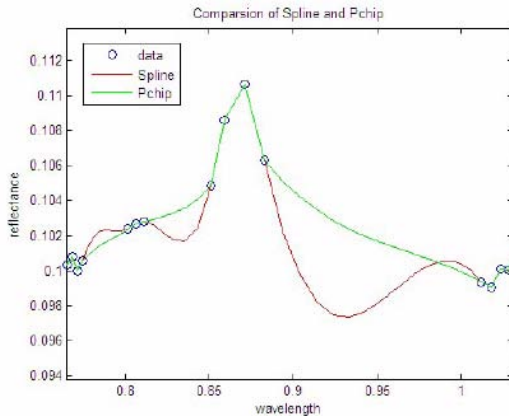\end{aligned} \qquad (6)
$$

$$
\begin{aligned}
H_{1;0}(\xi) &= 1 - 3\,\xi^2 + 2\,\xi^3 \\
H_{2;0}(\xi) &= 3\,\xi^2 - 2\,\xi^3 \\
H_{1;1}(\xi) &= \xi - 2\,\xi^2 + \xi^3 \\
H_{2;1}(\xi) &= -\xi^2 + \xi^3
\end{aligned} \qquad (7)
$$

where $\xi = (x - x_i) \, / \, (x_{i+1} - x_i)$.

Spline may tend to have oscillation as seen in Figure 4 due the way the algorithm tries to fix the data. PCHIP does not suffer these oscillations since PCHIP finds the slope which does not cause an overshoot. PCHIP increases, decreases and stays constant with data as seen in Figure 5.

Figure 4. Interpolation of truncated data using different methods.
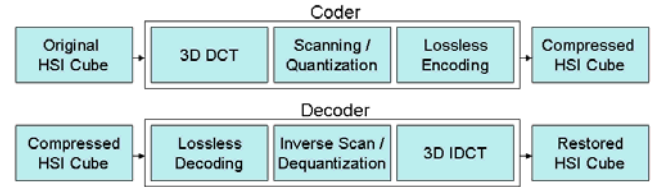

Figure 5. Comparison of Spline and PCHIP interpolation showing oscillations.

While interpolation is conducted, it must be done in coordination with the compression method.

4   HSI Compression

4.1 HSI Compression Codec

The compression scheme developed in this paper is modeled after similar compression schemes used in JPEG and MPEG. There are many other compression techniques [9-13] from which we seek to explore further comparisons. The block diagram illustrating the main codec components can be seen in Figure 6. The codec relies on the energy compaction ability of the discrete cosine transform (DCT) and attenuates low energy coefficients and uses quantization as a roundoff process. The results of the quantization are then put through lossless compression algorithms.
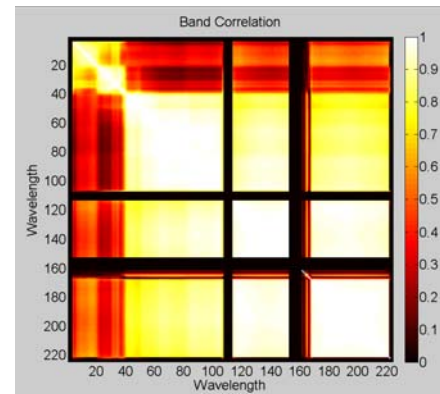

Figure 6. Block diagram of HSI Compression Codec

Processing begins by segmenting the HSI data cube into smaller cubes of 8×8×8. After a volume is segmented, it is then processed through the diagram with 3D compression, scanning/quantization, and encoding, illustrated in Figure 6.

4.2 3D Discrete Cosine Transformation

The 3D discrete cosine transform (DCT) is a linear unitary transform that is similar to the discrete Fourier transform (DFT) but differs by representing a signal in real terms as opposed to complex. The DCT is a popular choice for transform coding of images because most of the pixels in images show a high correlation between neighboring pixels. HSI data, radiance or reflectance, tends to also be highly correlated between wavelength bands so the DCT should apply equally as well to the third wavelength dimension, see Figure 7.

Figure 7. Correlation between bands of Moffett Field data cube. Black regions represent unusable bands in data cube.

A property of the DCT that lends itself to performing well on images, highly correlated signals, is that the DCT coefficients are uncorrelated which infers that the DCT shows a strong *decorrelation property* [16]. In addition to excellent decorrelation the DCT is able to compact energy into the lower frequencies so that the signal can be represented with fewer coefficients [17]. The 1D DCT is defined by

$$D(u) = \alpha(u) \sum_{x=0}^{N-1} f(x) g(x,u) \qquad (8)$$

for $u = 0, 1, 2, \ldots, N-1$. Similarly the inverse DCT (IDCT) is defined as

$$f(x) = \alpha(u) \sum_{u=0}^{N-1} D(u) \cos\left(\frac{\pi(2x+1)u}{2N} \right) \qquad (9)$$

for $x = 0, 1, 2, \ldots, N-1$. In both of the previous equations $\alpha(u)$ is defined as

$$\alpha(u) = \begin{cases} 1/\sqrt{N}, & u = 0 \\ \sqrt{2/N}, & 1 \le u \le N-1. \end{cases} \qquad (10)$$

and the transform kernel $g(x, u)$ is defined as

$$g(x,u) = \cos \frac{\pi(2x+1)u}{2N}. \qquad (11)$$

The DCT, like the DFT, is separable and can be used in a multidimensional transform by applying the 1D transform along each dimension [16]. The 3D DCT transform becomes

$$D(u,v,w) = A \sum_{x=0}^{L-1} \sum_{y=0}^{M-1} \sum_{z=0}^{N-1} f(x,y,z) G \qquad (12)$$

where

$$A = \alpha(u)\alpha(v)\alpha(w) \qquad (13)$$

and

$$G = g(x,u) g(y,v) g(z,w). \qquad (14)$$

4.3 Scanning/Quantization

After the 3D DCT has been performed, a scanning function is used to convert the 3D volume into a 1D array of DCT coefficient values. The ideal scanning function would essentially convert the cube into a sorted list of coefficients. Two methods were used in the scanning process. The first method involved *scanning the 3D cube of coefficients into a 1D vector* and then applying the quantization. The scanning was done using a zig-zag scan, similar to JPEG, and then quantization was applied. The quantization vector was based on an exponential function where the time constant was varied to increase or decrease the compression ability of the quantized signal. Figure 8 illustrates the scanning and quantization process The last

part of the scanning process involves turning the 2D matrix representation show in the bottom of Figure 8 into a 1D vector by concatenating each row to the previous.
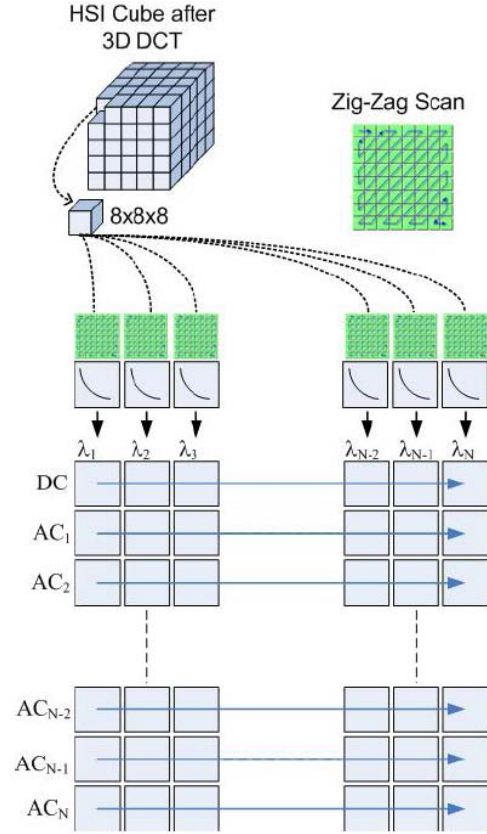

Figure 8. Block diagram of HSI Compression Codec

The second method involved using a scanning function found in [21]. The analog channel (AC) luminance and chrominance coefficients tend to have a Laplacian distribution centered about the mean with the largest magnitudes closest to the main axes [21]. To take advantage of the coefficient distribution a hyperboloid function was used to determine the scanning order [21].

$$q = A\left(1 - \frac{e^{-\beta((u+1)(v+1)(w+1))}}{e^{-\beta}} \right) + 1 \qquad (15)$$

$$A = 255, \ \beta = 0.00001$$

The function was tuned by finding optimal values for A and β and by weighting each axis (u, v, w) to determine the scan order.

The results from the scanning were then quantized to values between 0 and 255 with the higher frequency coefficients set to 0. The number of coefficients that are zeroed depends upon the level of compression required. Zeroing of the coefficients creates a lossy compression by creating runs of zeros in the sequence that cannot be retrieved in the decoding process. Utilizing this approach, a sensor manager could dictate the compression related to needed classification accuracy.
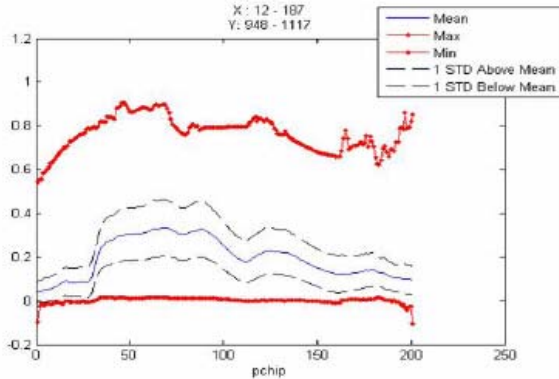
4.4 Lossless Encoding

The lossless encoding consists of two parts. The first part takes the 1D vector from scanning/quantization and performs a *run length encoding*. The run length encoder is beneficial because many of the AC coefficients are quantized to zero creating numerous runs in the data. The run length algorithm used only encodes runs of three or more which prevents bloating of the uncorrelated data. The last phase of the compression process involves using a Huffman coder to compress the result from the run length encoding. The *Huffman coding* is an entropy coder that performs a lossless compression by building a binary tree based on source symbol occurrences. Results have shown that arithmetic coding often outperforms the Huffman algorithm but was not selected due to its computational complexity. A more detailed treatment of Huffman coding can be found in [22].

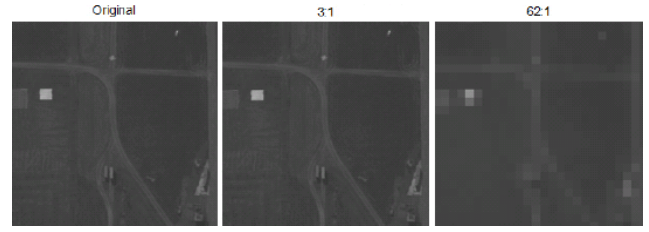## 5 Results

5.1 HYDICE

The HSI data used for this project was provided by Naval Research Lab (NRL). This data was from the Hyperspectral Digital Imagery Collection Experiment (HYDICE) with each pixel representing approximately a 2×2 meter square and 210 bands per sample.

The HSI data was modified by truncating band associated with water absorption. These cuts and any other discontinuities were filled with interpolated data generated through PCHIP. Figure 9 shows the results of one of these interpolations.

Figure 9. Example of interpolated spectral data after truncation.

The compression results can be seen in Figure 10 where the original image can be compared to many different compressions ratios. From Figure 10, we can see that environmental targets (i.e. roads) are identifiable at different compression ratios. The target resolution (pixels on target) would vary for classification, but detection is maintained.

Figure 10. Image compression showing maintained target detection through frequency fusion.

Information fusion evaluation is based on the metrics chosen. Likewise, the results can be utilized in a performance model (i.e. exploitation) that a sensor manager (SM) can use to route sensors, predict target classification, and call for multiple looks on targets. An example of a SM tradeoff is for a given throughput size (data rate), *does it take multiple low resolution images or a single high resolution image*? Besides the visual comparison in Figure 10, a statistical measure involving the peak signal to noise ratio (PSNR) which can be calculated based on the following equations.
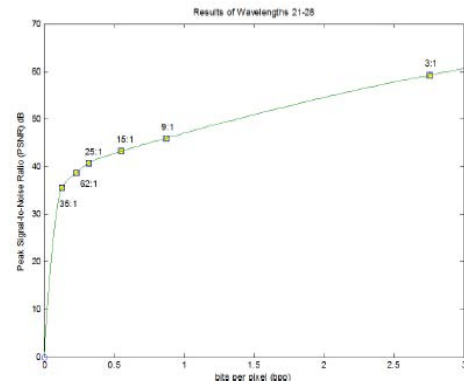
$$MSE = \frac{1}{mnp}\sum_{i=0}^{m-1}\sum_{j=0}^{n-1}\sum_{k=0}^{p-1}\left[I_{ijk} - C_{ijk}\right]^2 \quad (16)$$

$$PSNR = 20\log_{10}\left(\frac{255}{\sqrt{MSE}}\right) \quad (17)$$

The PSNR values and compression ratios are shown in Table 1 and a plot of PSNR against the bits per pixel (bpp) is shown in Figure 11, which can be used as a *performance model* over target detection.

Table I – 3D DCT Compression Results (HYDICE)

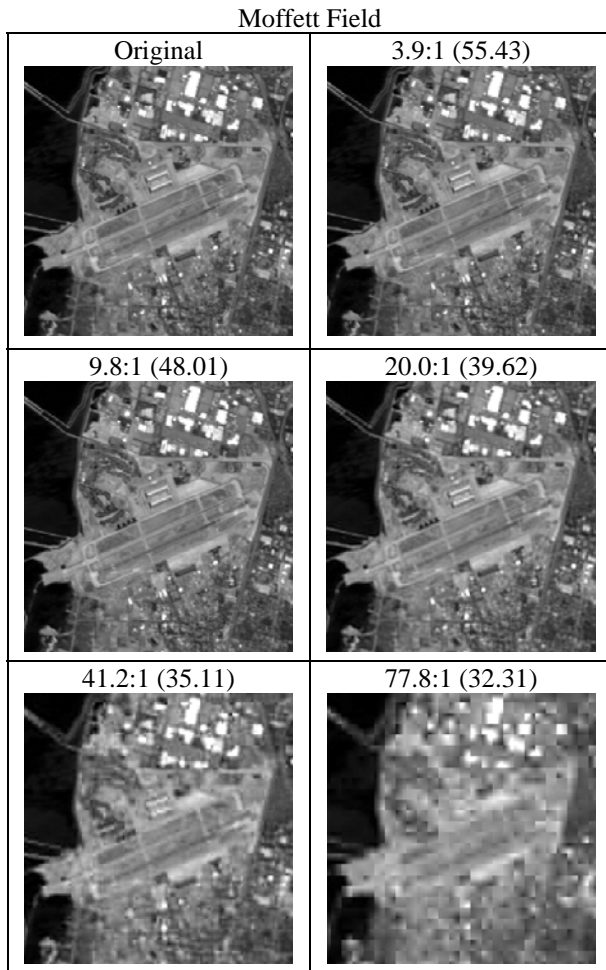| PSNR	Compression Ratio	bpp
59.3	2.9:1	2.76
46.0	9.2:1	0.87
43.2	14.5:1	0.55
40.8	25.0:1	0.32
38.7	34.6:1	0.23
35.5	62.1:1	0.13

Figure 11. PSNR vs. bits per pixel

5.2 NASA AVIRIS

To enhance the robust performance analysis, a second data set was run to evaluate the algorithm. The algorithm used on the AVIRIS dataset involved deleting the junk bands instead of interpolating across the bad regions. One issue that arises from deleting the bands is that discontinuities are introduced the spectral bands. Since the basis functions for the DCT are sinusoidal the transformed representation requires higher frequency coefficients to represent the signal. This introduces ringing in the transformation and degrades the compression quality across the discontinuities.

Moffett Field

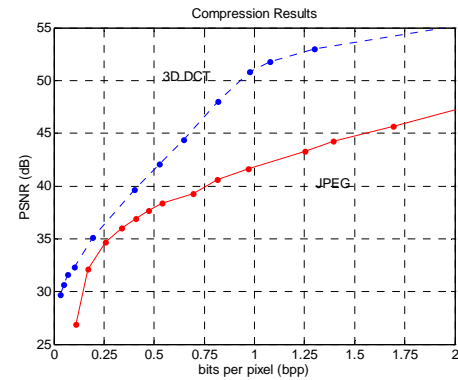
Figure 12. Compression Results (Band 120)

We conveniently resolved this issue by discarding extra bands so that the boundary of the processing did not overlap the discontinuity. Wavelet transforms have been shown to minimize the resultant discontinuities [1]. The compression results can be seen in Figure 12 where the original image can be compared to various levels of compression.

The PSNR values and compression ratios are shown in Table 2 and a plot of PSNR against the bits per pixel (bpp) is shown in Figure 13. The 3D DCT compression yielded better results than the baseline JPEG compression with the PSNR near 10 dB greater near one bit per pixel. It is important to note that this data set is more rich in features, however, a simple detection was used only for the runway and large buildings. Further work will determine the tradeoff of compression to classification over the varying target size (which is not yet in the literature as the geoscience community has only looked at large blobs and area classification versus target classification.)

Table 2 – 3D DCT Compression Results (AVIRIS)

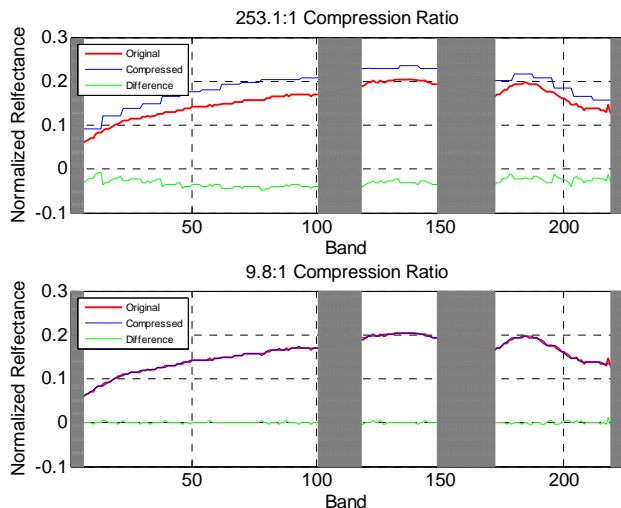| PSNR	Compression Ratio	bpp
29.70	253.1:1	0.032
30.63	159.7:1	0.050
31.58	113.9:1	0.070
32.31	77.8:1	0.103
35.11	41.2:1	0.194
39.62	20.0:1	0.401
42.06	15.2:1	0.527
44.38	12.4:1	0.647
48.01	9.8:1	0.819
50.81	8.2:1	0.978
51.80	7.4:1	1.076
53.00	6.2:1	1.299
55.43	3.9:1	2.076

Figure 13. Top line shows result of using the 3D DCT compression against the baseline result of JPEG.

To simultaneously evaluate detection, compression, and interpolation, Figure 14 shows the compression ratio over various bands. The method allows for variable compression rates to correspond to efficient spatio/temporal/spectral constraints. A key to note, and a goal of this work, is to look at the compression and detection (classification) where the sensor processing truncates the data. The truncated bands will have classification consequences as the lack of information could alter the target-ground contrast. Being able to interpolate these bands while reducing the data (throughput) size is important for future fusion of classifiers and sensor management research.

581

In addition to the static case presented, future evaluations will be performed over different classifiers such as mutual information [23] and be applied to frames [24] for a HSI simultaneous tracking and identification.

Figure 14. Reflectance plot for an arbitrarily selected pixel for two compression ratios, 253.1:1 and 9.8:1. (Shaded regions represent junk bands)

6 Conclusions

The goal provided an information fusion performance evaluation over spatio/spectral throughput, detection, classification, and data performance which can be utilized by a sensor manager for performance optimization. We improved standard compression techniques (i.e. JPEG) by finding a scanning algorithm that more efficiently maintained the high value DCT coefficients in conjunction with quantization as well as utilized interpolation methods for exploitation. Future sensor management strategies of HSI include multiple-frame processing [25], routing and pointing the platform and sensor, selective compression over bands of interest based on the target material type for classification, and interpolation across bands with distortion. Together, the simultaneous optimization of these functions would afford robust performance (effective and efficient); with appreciation of the scenarios of interests including the sensors, targets, and environmental conditions such as dictating the compression related to needed classification accuracy.

7 References

[1] AVIRIS Airborne Geoscience Workshop Proceedings ftp://popo.jpl.nasa.gov/pub/docs/workshops/aviris.proceedings.html, 1998 – 2004.

[2] http://dynamo.ecn.purdue.edu/~biehl/MultiSpec/.

[3] C. Lee & D. Landgrebe, "Decision boundary feature extraction for neural networks. *IEEE Trans. on Neural Networks,* vol. 8, 1997.

[4] D. Landgrebe, "Multispectral Data Analysis: A Signal Theory Perspective," 1998. (on line)

[5] C-I Chang. *Hyperspectral Imaging: Techniques for Spectral Detection and Classification.* Kluwer, New York, 2003.

[6] M. T. Eismann and D. W. Stein, "Stochastic Mixture Modeling", Ch. 5 in *HSI Data Exploitation: Theory and Applications.* Ed. C-I Chang, John Wiley., 2007.

[7] X. R. Wang, A. J. Brown, B. Upcroft, "Applying Incremental EM to Bayesian Classifiers in the Learning of HSI Remote Sensing Data," *Fusion05*, 2005.

[8] M. Fauvel, J. Chanussot, and J. A. Benediktsson "Decision Fusion for Hyperspectral Classification", Ch. 12 in *Hyperspectral Data Exploitation: Theory and Applications.* Ed. C-I Chang, John Wiley & Sons, Inc., 2007.

[9] G.P. Abousleman, M.W. Marcellin and B.R. Hunt, "Compression of Hyperspectral Imagery Using 3-d DCT and Hybrid DPCM/DCT", *IEEE Trans. Geosci. Remote Sensing*, Vol. 33, pp. 26-34, Jan. 1995.

[10] G. Motta, F. Rizzo, and J. Storer (eds.), *Hyperspectral Data Compression,* Springer, 2006.

[11] E. Christphe, C. Mailhes, and P. Duhamel, "Hyperspectral Image Compression: Adapting SPIHT and EZW to Anisotropic 3D Wavelet Coding," *IEEE Trans. On Image Processing*, 2006.

[12] S. Qian *et al*, "Near Lossless Data Compression onboard a Hyperspectral Satellite," *IEEE Trans. AES*, Vol. 42, 2006.

[13] J. E. Fowler and J. T. Pucker "Three-Dimensional Wavelet-based Compression of Hyperspectral Imagery", Ch. 14 in *Hyperspectral Data Exploitation: Theory and Applications.* Ed. C-I Chang, John Wiley & Sons, Inc., 2007.

[14] M. J. Mendenhall and E. Merenyi, "Relevance-based Feature Extraction from Hyperspectral Images in the Complex Wavelet Domain," *IEEE SMC Conf*, 2006.

[15] G. Mercier and M. Lennon, "Joint Classification and Compression of Hyperspectral Image" Ch 7 in *Hyperspectral Data Compression*, (Eds.) G. Motta, F. Rizzo, and J. Storer, Springer, 2006.

[16] K. Rao and P. Yip, *Discrete Cosine Transform: Algorithms, Advantages, and Applications*. Academic Press, Inc., 1990.

[17] S. Khayam, "The Discrete Cosine Transform (DCT): Theory and Application," *WAVES lab technical report*, May 2004.

[18] J. Kerekes and J. R. Schott, "Hyperspectral Imagining Systems", Ch. 2 in *HSI Data Exploitation: Theory & Applications.* Ed. C-I Chang, John Wiley & Sons, 2007.

[19] NASA AVIRIS Hyperspectral Data Sets and Information: http://aviris.jpl.nasa.gov/html/aviris.freedata.html

[20] Zelinski, A. C. and Goyal, V. K., "Denoising Hyperspectral Imagery and Recovering Junk Bands using Wavelets and Sparse Approximation," *Proc. IEEE ICCAD*, 2004.

[21] Podrikidis, C., *Numerical Computation in Science and Engineering*, Oxford Press, 1998.

[22] R. K.W. Chan and M.C. Lee, "3D-DCT Quantization as a Compression Technique for Video Sequences," *1997 Int. Conf. on Virtual Sys. & MultiMedia*, 1997.

[23] A. Drozdek, *Data Structures and Algorithms in C++,* 2nd ed., Pacific Grove: Brooks/Cole, 2001.

[24] B. Gui. S. Gunn, B. Damper, & J. Nelson, "Adaptive Band Selection for HSI Fusion Using Mutual Information," *ISIF Conf, Fusion05*, 2005.

[25] X. Li and B. Furht, "An Approach to Image Compression Using Three-Dimensional DCT," Proc. *6th Int'l. Conf. on Visual Information System* (VIS2003), 2003.